

Robust quantum anomalous Hall effect with spatially uncorrelated disorder

Kristof Moors^{1,2,*} and Gen Yin^{3,†}

¹*Peter Grünberg Institute (PGI-9), Forschungszentrum Jülich, 52425 Jülich, Germany*

²*JARA-Fundamentals of Future Information Technology, Jülich-Aachen Research Alliance, Forschungszentrum Jülich and RWTH Aachen University, 52425 Jülich, Germany*

³*Department of Physics, Georgetown University, Washington, D.C. 20057, USA*

(Dated: May 7, 2025)

In magnetic topological insulators, a phase transition between quantum anomalous Hall (QAH) and Anderson localization insulating phases can be triggered by the rotation of an applied magnetic field. Without the scattering paths along magnetic domains, this phase transition is governed by scattering induced by nonmagnetic disorder. We show that the QAH phase is strikingly robust in the presence of spatially uncorrelated disorder. The robustness is attributed to a resilience of the topological band gap against disorder, induced by quantum confinement. The critical behavior near the phase transition suggests that the scattering is distinct from quantum percolation. This provides new insights on the robustness of the QAH effect in magnetic topological insulators with atomic defects, impurities, and dopants.

Magnetic topological insulator (MTI) thin films have received a lot of attention as a host of the quantum anomalous Hall (QAH) effect [1–4]. This stems from the dissipationless transport of a topologically protected edge channel for which backscattering is strictly forbidden. This edge channel is promising for various applications due to its quantum coherent nature, especially as an important building block of topological superconductors hosting chiral Majorana modes [5]. An ideal QAH system has the Fermi level inside the QAH gap across the whole sample, but energy fluctuations due to disorder are inevitable in real systems. For example, in magnetically modulated $(\text{Bi,Sb})_2\text{Te}_3$, the doping with Sb atoms is essential, dragging the Fermi level down to the center of the bulk band gap [2, 6, 7]. Magnetic dopants such as Cr, Mn and V are usually added to replace the Bi sites, offering the long-range magnetic order that opens up a topological band gap near the Dirac point of the surface states [8, 9]. Characterized by scanning tunneling microscopy, the spatial correlations of the disorder are typically at the atomic scale or up to a few nanometers [10–13] and the energy fluctuation can be up to ~ 0.1 eV [14]. Surprisingly, the QAH effect can still emerge at low temperatures (~ 1 K), and the quantization is robust and accurate.

A typical measurement of the QAH effect is performed by scanning the out-of-plane magnetic field. When lowering the field, the magnetization originally along the out-of-plane easy axis shrinks, which lowers the topological band gap and eventually drives the system into an Anderson localized insulating state (ALI), yielding a quantum phase transition. Several theoretical works have already studied the properties of this transition in MTI thin films with magnetic and nonmagnetic disorders [15–18]. Interestingly, this transition is similar to plateau transitions in

quantum Hall systems [19, 20], which display universal properties that are manifested by the critical behavior of quantum percolation [21, 22]. In recent experimental studies, the value of the scaling exponent has been reported to vary in a range ($\nu \approx 2.7$ in Ref. [23], $\nu \approx 1.6$ in Ref. [24]), suggesting the rich underlying physics. Recent theoretical studies have also pointed out that the domain walls formed near the coercive field can host extra topological edge modes, resulting in a Berezinskii-Kosterlitz-Thouless-type transition in the presence of structural inversion asymmetry [25].

In this work, we closely examine the quantum phase transition in MTI thin films induced by a rotation of the external magnetic field, rather than a linear scan [23, 26, 27]. With this approach, the magnetization can be dragged along the external magnetic field, avoiding the formation of magnetic domains. The topological band gap eventually closes when the magnetization is completely in-plane. Although the scattering paths provided by magnetic domains are absent in this setup, nonmagnetic disorder can still drive the system into an ALI phase [6, 7, 17, 23, 24, 26–29]. Here, we show that the critical behavior of the phase transition strongly depends on the correlation length of the nonmagnetic disorder. In particular, when the spatial correlation length approaches the nanometer scale, the critical exponent deviates from the quantum percolation value ($\nu \approx 2.6$) and varies sensitively with the disorder strength. More importantly, the short correlation length preserves dissipationless transport even when the energy fluctuations significantly exceed the band gap of the clean limit, resulting in a quantized Hall conductivity that is unexpectedly robust.

We consider a two-dimensional four-orbital tight-binding model on a square lattice. This model is obtained from standard discretization of a four-band model of an MTI thin film [1, 5] with a lattice constant $a = 1$ nm:

$$H_{\text{MTI}}(k_x, k_y) = \hbar v_{\text{D}}(k_y \sigma_x - k_x \sigma_z) \tau_z + [m_0 - m_1(k_x^2 + k_y^2)] \tau_x + \mathbf{M} \cdot \boldsymbol{\sigma}, \quad (1)$$

* Present Address: Imec, Kapeldreef 75, 3001 Leuven, Belgium; kristof.moors@imec.be

† gen.yin@georgetown.edu

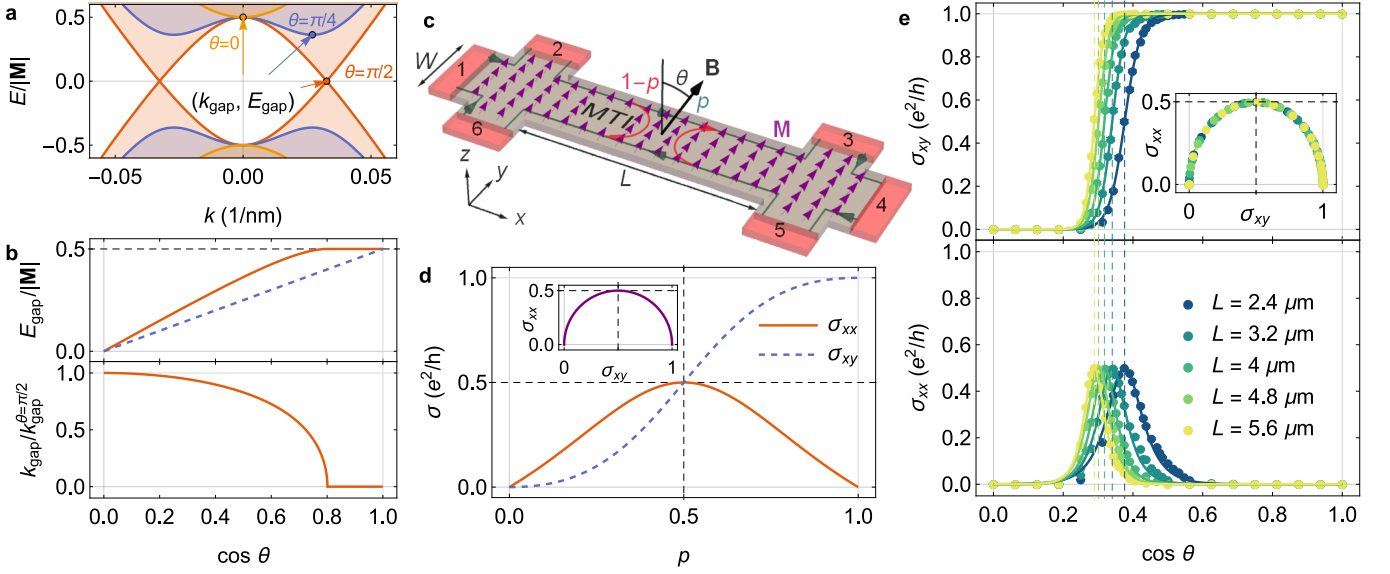


FIG. 1. **Magnetization rotation-driven QAH-to-trivial insulator transition in a MTI thin film.** (a) The spectrum of a MTI ribbon along k_x for different orientation angles θ of the magnetization in the y - z plane, with the spectral gap closing when the magnetization is directed along y ($\theta = \pi/2$). (b) The size and position in reciprocal space of the spectral gap as a function of $\cos \theta$. (c) Schematic of a MTI thin-film Hall bar in the single-channel regime with rotating magnetization angle θ and transmission probability p for a chiral edge channel across the central section of the Hall bar. (d) The longitudinal and Hall conductivities of the MTI Hall bar as a function of the transmission probability p , satisfying a semicircle relation (see inset). (e) The longitudinal and Hall conductivities for disordered MTI thin-film Hall bars ($E_F = 0.2 E_{\text{gap}}^{\theta=0}$, spatially uncorrelated disorder with $S_{\text{dis}} = 3 E_{\text{gap}}^{\theta=0}$, and y - z magnetization rotation plane) of different sizes (with identical aspect ratio $L/W = 80$) as a function of $\cos \theta$, based on microscopic quantum transport simulations (see text for details). The transition value $\cos \theta^*$ is indicated for the different ribbon sizes with a vertical dashed line.

where σ_i and τ_i ($i = x, y, z$) are the Pauli matrices acting on the spin up/down and top/bottom surface subspaces, respectively. The first term is the typical Rashba-Dirac term of TI surface states with Dirac velocity v_D . The bulk spectrum of the MTI is not included in the continuum model, but the coupling of the top and bottom surfaces through the bulk is governed by parameters m_0 and m_1 . The magnetization of the material is represented by the vector \mathbf{M} . In our quantum transport simulations, we consider the following parameters: $v_D = 3.5 \times 10^5$ m/s, $m_0 = 50$ meV, $m_1 = 15$ meV $\cdot\text{\AA}^2$ and $|\mathbf{M}| = 100$ meV. With an out-of-plane orientation of the magnetization, the system is a QAH insulator with a gap $2E_{\text{gap}}^{\theta=0} = 2|\mathbf{M}| - |m_0| = 100$ meV.

In this work, we consider a uniform (single-domain) magnetization across the MTI thin-film system with a fixed orientation and angle θ with respect to the z axis: $M_z = |\mathbf{M}| \cos \theta$. When the magnetization is rotated from out-of-plane to in-plane, the QAH gap reduces and eventually closes (see Figs. 1a,b and SUPPLEMENTAL NOTE 1). We restrict our setup to nonmagnetic disorder (i.e., spectral fluctuations due to, e.g., charged impurities or the electrostatic environment), which is introduced as fluctuations of the onsite energies δE_{onsite} . Disorder is described by a Gaussian distribution, $f(\delta E) = 1/\sqrt{2\pi S_{\text{dis}}^2} \exp[-\delta E^2/(2S_{\text{dis}}^2)]$ with disorder strength S_{dis} . For uncorrelated disorder, this dis-

tribution is applied independently on each lattice site. For spatially correlated disorder, the following autocovariance function is considered:

$$\langle \delta E(\mathbf{r}) \delta E(\mathbf{r}') \rangle = S_{\text{dis}}^2 \exp[-(\mathbf{r} - \mathbf{r}')^2 / (2\Lambda^2)], \quad (2)$$

with correlation length Λ . While disorder in lattice models of topological materials is commonly generated without spatial correlations [15, 17, 18, 30, 31], we find that these correlations can be of crucial importance with respect to the robustness of the QAH effect.

To capture the QAH effect in the modeled system, we perform quantum transport simulations implemented in Kwant [32], with the parallel sparse direct solver MUMPS [33]. In our simulations, we only consider disorder in the central section of the MTI between the left (1,2,6) and right (3,4,5) terminals (see Fig. 1c) such that the 6-terminal setup can be reduced to a two-terminal transport picture. The transmission probability p over the central section is extracted from a two-terminal scattering matrix. The longitudinal and Hall conductivities are therefore given by: $\sigma_{xx} = (e^2/h)(p-p^2)/[1+2p(p-1)]$ and $\sigma_{xy} = (e^2/h)p^2/[1+2p(p-1)]$, respectively (see Fig. 1d). Details of this setup can be found in SUPPLEMENTAL NOTE 2. Note that the conductivities satisfy the semicircle law [34–36]: $(\sigma_{xx}/\sigma_0)^2 + (\sigma_{xy}/\sigma_0 - 1/2)^2 = (1/2)^2$, where $\sigma_0 \equiv e^2/h$ is the quantized sheet conductivity. This can be seen from the inset of Fig. 1d. To

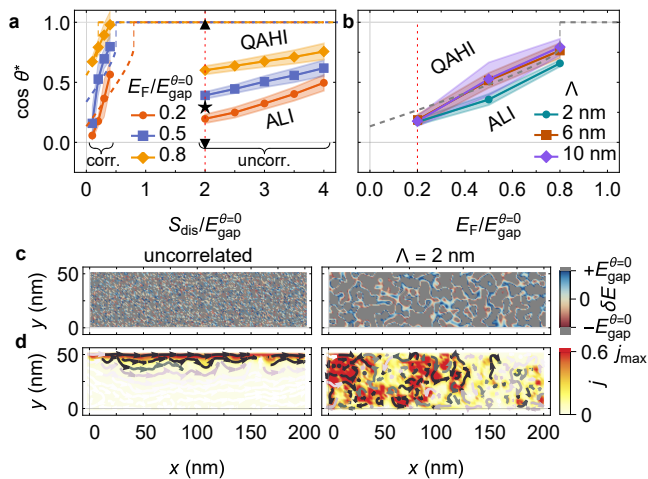


FIG. 2. **Robustness of QAH phase.** (a),(b) The transition value $\cos \theta^*$ (for magnetization rotated in the y - z plane) is shown for an MTI ribbon with $W = 0.05 \mu\text{m}$, $L = 4 \mu\text{m}$ (a) as a function of disorder strength for spatially correlated ($\Lambda = 10$ nm) and uncorrelated disorder with different Fermi levels and (b) as a function of Fermi energy for spatially correlated disorder with different correlation lengths and disorder strength $S_{\text{dis}} = 0.2 E_{\text{gap}}^{\theta=0}$. The shading around the data points displays the full width at half maximum of the longitudinal conductivity peak (see Fig. 1e) and reference values for the percolation threshold via quantum tunneling are indicated with dashed lines (see text for details). (c),(d) The (c) disorder potential (red-blue color scale indicating fluctuations with Fermi level remaining locally within the bulk gap, and gray otherwise) and (d) current density profile of a QAH edge channel that is injected from the left with energy $E_F = 0.2 E_{\text{gap}}^{\theta=0}$ (indicated with red dotted line in b and Fig. 3a) into a disordered MTI ribbon section with (y - z) rotated magnetization ($\cos \theta = 0.3$) and disorder strength $S_{\text{dis}} = 2 E_{\text{gap}}^{\theta=0}$ (also see Fig. 3a), considering (left) spatially uncorrelated and (right) spatially correlated disorder ($\Lambda = 2$ nm).

understand the critical behavior near the phase transition, one needs to find the parameters that cover both the quantized and the localized plateau. One set of such transition curves can be seen in Fig. 1e, where the Hall conductivity serves as the order parameter when we rotate the magnetization at an angle θ away from the z axis: $\cos \theta \in [0, 1]$. The transfer matrix method is then employed to extend the length of this central section beyond the length of the simulation domain, as described in SUPPLEMENTAL NOTE 3. Instead of doing a single simulation, we perform such simulations on $N_{\text{dis}} = 5000$ systems with different landscapes of disorder, and then extract the average transmission probability (see SUPPLEMENTAL NOTE 4). The transition curves are well described by a hyperbolic tangent profile, as shown by the lines through the data points in Fig. 1e. We use two fitting parameters to characterize the position of the transition, i.e., the transition value $\cos \theta^*$ with $\sigma_{xx}(\cos \theta^*) = \sigma_{xy}(\cos \theta^*) = e^2/(2h)$, and the

steepness of the transition, respectively (see SUPPLEMENTAL NOTE 5).

The transition between the QAH and ALI phases is sensitive to both the Fermi level position and the spatial correlation of the nonmagnetic disorder. We demonstrate this by extracting the transition values $\cos \theta^*$ of the phase transition for different system parameters. In Fig. 2, we present $\cos \theta^*$ for spatially correlated and uncorrelated disorder as a function of the Fermi level position (2a) and disorder strength (2b), while keeping other parameters identical. As expected, the QAH phase withstands larger out-of-plane orientation angles for a Fermi level that is more centrally positioned in the QAH gap (i.e., closer to the Dirac point) and for lower disorder strengths.

The QAH-ALI phase transition is expected to occur when the edge state is able to backscatter into the opposing counterpropagating state across the bulk, through a combination of scattering or quantum tunneling [22]. The transition can be expected near the condition $\mu \pm S_{\text{dis}} \pm E_{\text{gap}}(\cos \theta) = 0$, where the disorder strength aligns the local Fermi level with the band edge of the bulk spectrum above or below the QAH gap. This condition is denoted by the dashed curves in Figs. 2a-b. In both figures, the area above the dashed curves is expected to be the QAH phase and the other side should be the ALI phase. Note that this expected phase boundary does not depend on the correlation length of disorder. When the disorder is correlated, the phase boundary is indeed well captured by our numerical results, as shown by the points on the left of Fig. 2a and those in Fig. 2b.

Surprisingly, the phase diagram captured by our numerical results is significantly distinct from the conventional understanding when the disorder is uncorrelated. The QAH phase appears to be much more robust against spectral fluctuations and still survives even when the disorder strength is well above the expected percolation threshold. This is represented by the enlarged area of the QAH phase shown by the points on the right of Fig. 2a. Two example profiles of the local chemical potential due to the nonmagnetic disorder are shown in Fig. 2c, where the gray (red-white-blue) color scale indicates local fluctuations that (do not) exceed the bulk topological gap. The large gray area in Fig. 2c suggests that significant percolation is expected for both the uncorrelated (left) and the correlated case (right). Notably, the edge state can almost transmit perfectly through the uncorrelated disorder, whereas severe percolation and backscattering are captured in the case of correlated disorder ($\Lambda = 2$ nm).

The extra robustness of the QAH effect stems from the insensitivity of the bulk spectrum against uncorrelated disorder. To show this, we examine the density of states (DOS) of a system with periodic boundary condition, so that the topological edge states do not show up (see Fig. 3a). This DOS is given by an overall smearing factor of 2.5 meV for all the eigenstates of a simulation domain of $0.2 \times 0.05 \mu\text{m}^2$. The three panels correspond to different rotation angles of the magnetization. In all

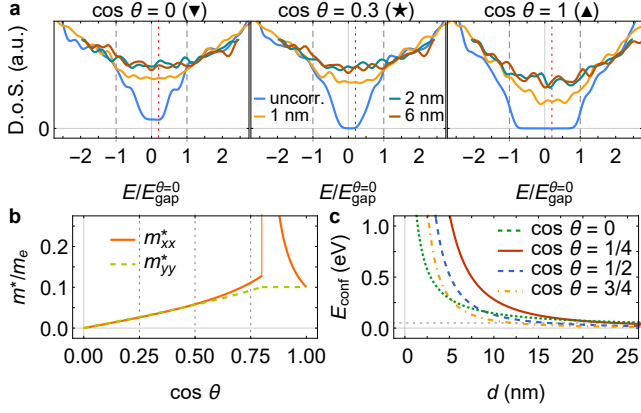


FIG. 3. **Robustness of spectral gap.** (a) The bulk density of states of a MTI thin film for different magnetization orientations and disorder correlation lengths with disorder strength $S_{\text{dis}} = 2E_{\text{gap}}^{\theta=0}$ (indicated by red dashed line in Fig. 2a). (b) The effective mass along x and y of the bulk spectrum minimum (see Fig. 1a and SUPPLEMENTAL NOTE 1) as a function of $\cos \theta$. (c) The confinement quantization energy of a bulk state as a function of the disorder puddle size d for different magnetization orientations (see gray dotted lines in b), with the bulk gap parameter $E_{\text{gap}}^{\theta=0}$ indicated by a gray dotted line (see text for details).

three cases, the disorder strength $S_{\text{dis}} = 2E_{\text{gap}}^{\theta=0}$ exceeds the bulk topological gap by a factor of two. For the correlated disorder, the topological gap closes in all three cases, as expected. However, the topological gap survives when the disorder is uncorrelated.

The resilience of the QAH gap against uncorrelated disorder can be understood by considering the confinement energy of the bulk states. At low energies, the bulk states are effectively trapped in regions $d \propto \Lambda$ due to disorder fluctuations (see, for example, the extent of the gray patches in Fig. 2c). This gives rise to a confinement energy that pushes up the energy levels by $E_{\text{conf}} \propto 1/d^2$, which is determined by the effective mass of the gap (or $\propto 1/d$ for massless states). We can extract the effective mass of the surface states from the curvature at the minimum of the spectrum (see Fig. 3b). The sudden jump near $\cos \theta \approx 0.76$ for m_{xx} is due to the band-edge transition from the two valleys (blue in Fig. 1a) to a direct band gap at Γ . In Fig. 3c, we roughly estimate the confinement energy for different patch sizes by considering hard-wall confinement along x and y . When the spectrum is massive (gapped), the confinement energy is given by the particle-in-a-box ground state, whereas the value for $\cos \theta = 0$ is given by the massless (gapless) solution $E_{\text{conf}} \approx 2\hbar v_D(\pi/d)$. It is clear that the confinement energy can easily exceed the QAH gap when the patch size is only a few nanometers. Furthermore, the confinement energy increases when the magnetization is rotated from out-of-plane to in-plane orientation, which enhances the confinement due to the reduction of the effective mass.

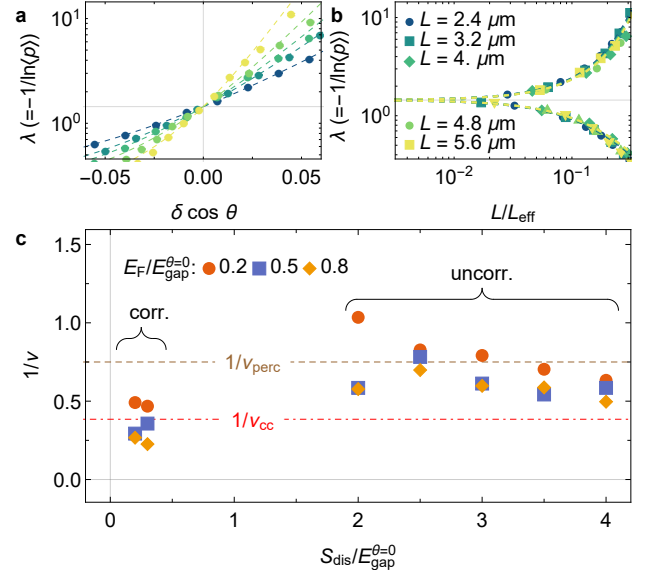


FIG. 4. **Finite-size scaling analysis of QAH-ALI phase transition.** (a) The localization length as a function of $\delta \cos \theta \equiv \cos \theta - \cos \theta^*$ for different MTI ribbon lengths. (b) The localization length as a function of MTI ribbon length normalized by the effective size L_{eff} , with single-parameter scaling relation $f(L/L_{\text{eff}})$ obtained from different MTI ribbon lengths with the MacKinnon-Kramer fitting procedure. (c) The inverse of the scaling exponent for the effective size ν ($L_{\text{eff}} \propto |\delta \cos \theta|^{-\nu}$) as a function of disorder strength for spatially correlated ($\Lambda = 10$ nm) and uncorrelated disorder. We consider an x - z magnetization rotation plane and show the results in a-b for spatially uncorrelated disorder with $E_F = 0.2E_{\text{gap}}^{\theta=0}$ and $S_{\text{dis}} = 2E_{\text{gap}}^{\theta=0}$.

The critical behavior of the QAH-ALI transition in the presence of uncorrelated disorder is fundamentally different from the case where the disorder is correlated. This can be demonstrated by different finite-size scaling behaviors at the transition. For this analysis, we consider the MacKinnon-Kramer fitting procedure [37] with dimensionless localization length $\lambda \equiv -1/\ln\langle p \rangle$, where $\langle p \rangle$ the ensemble-averaged transmission probability. The numerical results agree well with a single-parameter scaling of the localization length, $\lambda(L, \cos \theta) = f[L/L_{\text{eff}}(\cos \theta)]$, where $L_{\text{eff}}(\cos \theta) \propto |\delta \cos \theta|^{-\nu}$ and $\delta \cos \theta \equiv \cos \theta - \cos \theta^*$. We implemented a fitting procedure that directly yields the effective size scaling exponent ν (see SUPPLEMENTAL NOTE 6 for details) for different values of the Fermi level, disorder strength, and correlation length. As shown in Fig. 4a, λ as a function of $\delta \cos \theta$ crosses the same value when changing the size of the simulation domain, as expected. Furthermore, we can identify a power law $L_{\text{eff}}(\delta \cos \theta)$ that can collapse all the values of $\lambda(L, \cos \theta)$ on the same curve on both sides near the transition, as shown in Fig. 4b. The critical exponents are presented as a function of disorder strength in Fig. 4c and reference values for classical percolation ($\nu_{\text{perc}} = 4/3$) and quantum percolation according to the Chalker-Coddington

model [22] ($\nu_{CC} \approx 2.6$) are indicated by the horizontal dashed lines. For correlated disorder, the numerical exponent values reasonably agree with the Chalker-Coddington value. In this case, the transition occurs when the disorder strength is lower than the topological gap, where $S_{\text{dis}}/E_{\text{gap}}^{\theta=0} < 1$, which is also consistent with the quantum percolation picture. However, the exponent values display a pronounced dependence on the disorder strength when the disorder is uncorrelated. This suggests that the confinement not only introduces extra robustness to the QAH phase, but also modifies the quantum phase transition in a nonuniversal manner. Only for the largest disorder strengths is there a trend towards universal Chalker-Coddington-like scaling.

Besides the MacKinnon-Krammer approach, we also extracted the effective-size scaling exponent directly from fitting a power law to the size dependence of the maximal slope of the transition curve, which has been used in several recent experiments [23, 29], $\max\{d\sigma_{xy}/d\cos\theta\} \propto L^{1/\nu}$. The details of this approach are presented in **SUPPLEMENTAL NOTE 7** where we find good agreement with the results extracted by the MacKinnon-Kramer approach, indicating reasonable numerical stability. This also offers a straightforward indication of the correlation length of nonmagnetic disorder in QAH experiments, which can be tuned through various synthesis parameters, including substrate selection, doping levels, and dopant species.

Conclusion.—We have investigated the magnetization rotation-driven QAH-to-ALI phase transition in MTI

thin films with nonmagnetic disorder. Due to the confinement energy of low-energy bulk states that are effectively trapped in regions with size proportional to the disorder correlation length, the QAH phase is strikingly resilient with respect to atomic-scale disorder. The QAH phase withstands energy fluctuations significantly overwhelming the QAH gap, and the corresponding effective-size scaling exponent displays nonuniversal behavior. Our results shed new light on the robustness of the QAH effect in MTI thin films with uniformly random disorders at the atomic scale. This offers a new avenue in the search for ideal QAH systems besides clean and pristine Chern insulators.

Acknowledgments.—This paper is based upon work supported by the National Science Foundation (US) under Grant # ECCS-2151809 (G.Y.) and DMR-2440337 (G.Y.). This work is also supported by the QuantERA grant MAGMA and by the German Research Foundation under grant 491798118. K.M. acknowledges the financial support by the Ministry of Economic Affairs, Regional Development and Energy within Bavaria’s High-Tech Agenda Project “Bausteine für das Quantencomputing auf Basis topologischer Materialien mit experimentellen und theoretischen Ansätzen” (Grant No. 07 02/686 58/1/21 1/22 2/23), and by the German Federal Ministry of Education and Research (BMBF) via the Quantum Future project ‘MajoranaChips’ (Grant No. 13N15264) within the funding program Photonic Research Germany.

-
- [1] R. Yu, W. Zhang, H.-J. Zhang, S.-C. Zhang, X. Dai, and Z. Fang, *Science* **329**, 61 (2010).
 - [2] C.-Z. Chang, J. Zhang, X. Feng, J. Shen, Z. Zhang, M. Guo, K. Li, Y. Ou, P. Wei, L.-L. Wang, Z.-Q. Ji, Y. Feng, S. Ji, X. Chen, J. Jia, X. Dai, Z. Fang, S.-C. Zhang, K. He, Y. Wang, L. Lu, X.-C. Ma, and Q.-K. Xue, *Science* **340**, 167 (2013).
 - [3] Y. Tokura, K. Yasuda, and A. Tsukazaki, *Nat. Rev. Phys.* **1**, 126 (2019).
 - [4] Y. Deng, Y. Yu, M. Z. Shi, Z. Guo, Z. Xu, J. Wang, X. H. Chen, and Y. Zhang, *Science* **367**, 895 (2020).
 - [5] J. Wang, B. Lian, H. Zhang, Y. Xu, and S.-C. Zhang, *Phys. Rev. Lett.* **111**, 136801 (2013).
 - [6] X. Kou, L. Pan, J. Wang, Y. Fan, E. S. Choi, W.-L. Lee, T. Nie, K. Murata, Q. Shao, S.-C. Zhang, and K. L. Wang, *Nat. Commun.* **6**, 8474 (2015).
 - [7] J. G. Checkelsky, R. Yoshimi, A. Tsukazaki, K. S. Takahashi, Y. Kozuka, J. Falson, M. Kawasaki, and Y. Tokura, *Nat. Phys.* **10**, 731 (2014).
 - [8] M. Mogi, M. Kawamura, R. Yoshimi, A. Tsukazaki, Y. Kozuka, N. Shirakawa, K. S. Takahashi, M. Kawasaki, and Y. Tokura, *Nature Materials* **16**, 516 (2017), publisher: Nature Publishing Group.
 - [9] N. Liu, J. Teng, and Y. Li, *Nature Communications* **9**, 1282 (2018), publisher: Nature Publishing Group.
 - [10] I. Lee, C. K. Kim, J. Lee, S. J. L. Billinge, R. Zhong, J. A. Schneeloch, T. Liu, T. Valla, J. M. Tranquada, G. Gu, and J. C. S. Davis, *Proc. Natl. Acad. Sci.* **112**, 1316 (2015).
 - [11] Y. X. Chong, X. Liu, R. Sharma, A. Kostin, G. Gu, K. Fujita, J. C. S. Davis, and P. O. Sprau, *Nano Lett.* **20**, 8001 (2020).
 - [12] A. Park, A. Llanos, C.-I. Lu, Y. Chen, S. N. Abadi, C.-C. Chen, M. L. Teague, L. Tai, P. Zhang, K. L. Wang, and N.-C. Yeh, *Phys. Rev. B* **109**, 075125 (2024).
 - [13] J. Brede, M. Bagchi, A. Greichgauer, A. Uday, A. Bliesener, G. Lippertz, R. Yazdanpanah, A. Taskin, and Y. Ando, *Phys. Rev. Materials* **8**, 104202 (2024).
 - [14] C.-C. Chen, M. L. Teague, L. He, X. Kou, M. Lang, W. Fan, N. Woodward, K.-L. Wang, and N.-C. Yeh, *New Journal of Physics* **17**, 113042 (2015), publisher: IOP Publishing.
 - [15] M. Onoda and N. Nagaosa, *Phys. Rev. Lett.* **90**, 206601 (2003).
 - [16] K. Nomura and N. Nagaosa, *Phys. Rev. Lett.* **106**, 166802 (2011).
 - [17] C.-Z. Chang, W. Zhao, J. Li, J. K. Jain, C. Liu, J. S. Moodera, and M. H. W. Chan, *Phys. Rev. Lett.* **117**, 126802 (2016).
 - [18] Z. Qiao, Y. Han, L. Zhang, K. Wang, X. Deng, H. Jiang, S. A. Yang, J. Wang, and Q. Niu, *Phys. Rev. Lett.* **117**, 056802 (2016).
 - [19] *The Quantum Hall Effect* (Springer New York, 1990).
 - [20] B. Huckestein, *Rev. Mod. Phys.* **67**, 357 (1995).
 - [21] S. A. Trugman, *Phys. Rev. B* **27**, 7539 (1983).

- [22] J. T. Chalker and P. D. Coddington, *J. Phys. C* **21**, 2665 (1988).
- [23] M. Kawamura, M. Mogi, R. Yoshimi, A. Tsukazaki, Y. Kozuka, K. S. Takahashi, M. Kawasaki, and Y. Tokura, *Phys. Rev. B* **102**, 041301 (2020).
- [24] P. Deng, C. Eckberg, P. Zhang, G. Qiu, E. Emmanouilidou, G. Yin, S. K. Chong, L. Tai, N. Ni, and K. L. Wang, *Nat. Commun.* **13**, 4246 (2022).
- [25] C.-Z. Chen, H. Liu, and X. C. Xie, *Phys. Rev. Lett.* **122**, 026601 (2019).
- [26] M. Kawamura, M. Mogi, R. Yoshimi, A. Tsukazaki, Y. Kozuka, K. S. Takahashi, M. Kawasaki, and Y. Tokura, *Phys. Rev. B* **98**, 140404 (2018).
- [27] J. Luan, Y. Feng, Y. Ji, Y. Li, H. Li, Z. Liu, C. Liu, J. Zhang, X. Kou, and Y. Wang, *Phys. Rev. Lett.* **130**, 186201 (2023).
- [28] Y. Feng, X. Feng, Y. Ou, J. Wang, C. Liu, L. Zhang, D. Zhao, G. Jiang, S.-C. Zhang, K. He, X. Ma, Q.-K. Xue, and Y. Wang, *Phys. Rev. Lett.* **115**, 126801 (2015).
- [29] P. Deng, P. Zhang, C. Eckberg, S. K. Chong, G. Yin, E. Emmanouilidou, X. Che, N. Ni, and K. L. Wang, *Nat. Commun.* **14**, 5558 (2023).
- [30] J. Li, R.-L. Chu, J. K. Jain, and S.-Q. Shen, *Phys. Rev. Lett.* **102**, 136806 (2009).
- [31] C. W. Groth, M. Wimmer, A. R. Akhmerov, J. Tworzydło, and C. W. J. Beenakker, *Phys. Rev. Lett.* **103**, 196805 (2009).
- [32] C. W. Groth, M. Wimmer, A. R. Akhmerov, and X. Waintal, *New J. Phys.* **16**, 063065 (2014).
- [33] P. R. Amestoy, I. S. Duff, J.-Y. L'Excellent, and J. Koster, *SIAM J. Matrix Anal. Appl.* **23**, 15 (2001).
- [34] A. M. M. Pruisken, *Phys. Rev. Lett.* **61**, 1297 (1988).
- [35] A. M. Dykhne and I. M. Ruzin, *Phys. Rev. B* **50**, 2369 (1994).
- [36] M. Hilke, D. Shahar, S. H. Song, D. C. Tsui, Y. H. Xie, and M. Shayegan, *Europhys. Lett.* **46**, 775 (1999).
- [37] A. MacKinnon and B. Kramer, *Z. Phys. B Condens. Matter* **53**, 1 (1983).

**Supplemental Material: Robust quantum anomalous Hall phase
in magnetic topological insulators with atomic-scale disorder**

Kristof Moors^{1,2} and Gen Yin³

¹ *Peter Grünberg Institute (PGI-9), Forschungszentrum Jülich, 52425 Jülich, Germany*

² *JARA-Fundamentals of Future Information Technology, Jülich-Aachen Research Alliance,
Forschungszentrum Jülich and RWTH Aachen University, 52425 Jülich, Germany*

³ *Department of Physics, Georgetown University, Washington, D.C. 20057, USA*

SUPPLEMENTAL NOTE 1. SPECTRUM OF MTI MODEL HAMILTONIAN

The bulk spectrum of Eq. (1) of the Main Text with magnetization oriented in the y - z plane ($\mathbf{M} = |\mathbf{M}|(0, \sin \theta, \cos \theta)$) is given by:

$$E_{\mu,\nu}(k_x, k_y) = \mu \left(\hbar^2 v_D^2 k^2 + |\mathbf{M}|^2 + (m_0 - m_1 k^2)^2 + \nu |\mathbf{M}| \sqrt{2\hbar^2 v_D^2 k^2 (1 + \cos(2\theta)) + 4(m_0 - m_1 k^2)^2} \right)^{1/2}, \quad (\text{S1})$$

$$k^2 \equiv k_x^2 + k_y^2, \quad \mu, \nu = \pm 1. \quad (\text{S2})$$

The two lowest-energy bands ($\mu = \pm 1, \nu = -1$) are shown in Fig. 1a of the Main Text for different magnetization rotation angles θ . With in-plane orientation ($\theta = \pi/2$), the gap closes at $k_x = \pm(2m_0m_1 - \hbar^2 v_D^2 + \sqrt{\hbar^4 v_D^4 + 4m_1^2 |\mathbf{M}|^2 - 4m_0m_1 \hbar^2 v_D^2})^{1/2} / \sqrt{2m_1^2}$. The phenomenology remains similar when the magnetization is rotated along another in-plane direction.

SUPPLEMENTAL NOTE 2. CONDUCTANCE MATRIX

The conductance matrix G_{ij} (such that $I_i = \sum_j G_{ij} \delta\mu_j$ with $\delta\mu_1 = -\delta\mu_4 = \delta\mu/2$, $I_2 = I_3 = I_5 = I_6 = 0$, and I_i and $\delta\mu_i$ the current and chemical potential offset at terminal i , respectively) of the Hall setup with indexed leads in Fig. 1c has the following components:

$$G_{ij} = \frac{e^2}{h} \times \begin{cases} T_{ij} & (i \neq j) \\ -\sum_{k \neq i} T_{ik} & (i = j) \end{cases}, \quad (\text{S3})$$

$$T_{ij} = \begin{cases} 1 & (i, j) = (2, 1), (4, 3), (5, 4), (1, 6) \\ p & (i, j) = (3, 2), (6, 5) \\ 1 - p & (i, j) = (6, 2), (3, 5) \\ 0 & \text{else} \end{cases}, \quad (\text{S4})$$

for a chiral edge channel circling counterclockwise around the sample. With opposite chirality, the indices i and j should be swapped. Solving for $(I_1, I_4, \delta\mu_2, \delta\mu_3, \delta\mu_5, \delta\mu_6) \equiv (\mathbf{I}_{\text{lhs}}, \delta\boldsymbol{\mu}_{\text{lhs}})$, we obtain:

$$\begin{pmatrix} \mathbf{I}_{\text{lhs}} \\ \frac{e^2}{h} \delta\boldsymbol{\mu}_{\text{lhs}} \end{pmatrix} = \begin{pmatrix} I_{2 \times 2} & -\mathcal{T}_{2 \times 4} \\ 0 & \mathcal{T}_{4 \times 4} \end{pmatrix}^{-1} \begin{pmatrix} \mathcal{T}_{2 \times 2} & 0 \\ -\mathcal{T}_{4 \times 2} & I_{4 \times 4} \end{pmatrix} \begin{pmatrix} \frac{e^2}{h} \delta\boldsymbol{\mu}_{\text{rhs}} \\ \mathbf{I}_{\text{rhs}} \end{pmatrix}, \quad (\text{S5})$$

with

$$(\delta\boldsymbol{\mu}_{\text{rhs}}, \mathbf{I}_{\text{rhs}}) \equiv (\delta\mu_1, \delta\mu_4, I_2, I_3, I_5, I_6), \quad (\text{S6})$$

$$\mathcal{T}_{2 \times 2} \equiv \begin{pmatrix} -\sum_{i \neq 1} T_{1i} & T_{14} \\ T_{41} & -\sum_{i \neq 4} T_{4i} \end{pmatrix}, \quad (\text{S7})$$

$$\mathcal{T}_{2 \times 4} \equiv \begin{pmatrix} T_{12} & T_{13} & T_{15} & T_{16} \\ T_{42} & T_{43} & T_{45} & T_{46} \end{pmatrix}, \quad (\text{S8})$$

$$\mathcal{T}_{4 \times 4} \equiv \begin{pmatrix} -\sum_{i \neq 2} T_{2i} & T_{23} & T_{25} & T_{26} \\ T_{32} & -\sum_{i \neq 3} T_{3i} & T_{35} & T_{36} \\ T_{52} & T_{53} & -\sum_{i \neq 5} T_{5i} & T_{56} \\ T_{62} & T_{63} & T_{65} & -\sum_{i \neq 6} T_{6i} \end{pmatrix}, \quad (\text{S9})$$

$$\mathcal{T}_{4 \times 2} \equiv \mathcal{T}_{2 \times 4}^\top. \quad (\text{S10})$$

For our setup, the resistivity tensor has two independent components, $\rho_{xx} = \rho_{yy}$ and $\rho_{xy} = \rho_{yx}$, which can be defined in terms of the solutions \mathbf{I}_{lhs} and $\delta\boldsymbol{\mu}_{\text{lhs}}$ as follows:

$$\rho_{xx} = \frac{\delta\mu_3 - \delta\mu_2}{I_1}, \quad \rho_{xy} = \frac{\delta\mu_2 - \delta\mu_6}{I_1}. \quad (\text{S11})$$

From these resistivities, we can also obtain the longitudinal (σ_{xx}) and Hall (σ_{xy}) conductivities:

$$\sigma_{xx} = \frac{\rho_{xx}}{\rho_{xx}^2 + \rho_{xy}^2} = \frac{(\delta\mu_3 - \delta\mu_2)I_1}{(\delta\mu_2 - \delta\mu_6)^2 + (\delta\mu_3 - \delta\mu_2)^2}, \quad \sigma_{xy} = \frac{\rho_{xy}}{\rho_{xx}^2 + \rho_{xy}^2} = \frac{(\delta\mu_2 - \delta\mu_6)I_1}{(\delta\mu_2 - \delta\mu_6)^2 + (\delta\mu_3 - \delta\mu_2)^2}. \quad (\text{S12})$$

Plugging in Eq. (S4), we obtain:

$$\sigma_{xx} = \frac{p - p^2}{1 + 2p(p - 1)} \frac{e^2}{h}, \quad \sigma_{xy} = \frac{p^2}{1 + 2p(p - 1)} \frac{e^2}{h}. \quad (\text{S13})$$

SUPPLEMENTAL NOTE 3. TRANSFER MATRIX METHOD

To artificially extend the length of our simulated system, we consider the transfer matrix method. Starting from a generic 2-by-2 scattering matrix for an MTI ribbon with width W and length L with single chiral edge channel as input and output in the leads,

$$S = \begin{pmatrix} s_{L \leftarrow L} & s_{L \leftarrow R} \\ s_{R \leftarrow L} & s_{R \leftarrow R} \end{pmatrix} \quad (\text{S14})$$

with four complex values depending on the system and its microscopic details (e.g., disorder landscape). The transmission probability is given by $p = |s_{L \leftarrow R}|^2 = |s_{R \leftarrow L}|^2$. The scattering matrix connects the input states of the left and right leads to the corresponding output states: $(|o_L\rangle \ |o_R\rangle)^T = S(|i_L\rangle \ |i_R\rangle)^T$, where left and right input (output) states are $|i_{L,R}\rangle$ ($|o_{L,R}\rangle$), respectively. We can rewrite the scattering relation in terms of the transfer matrix M :

$$\begin{pmatrix} |i_R\rangle \\ |i_L\rangle \end{pmatrix} = M \begin{pmatrix} |i_L\rangle \\ |o_L\rangle \end{pmatrix} \quad \rightarrow \quad M = \begin{pmatrix} -s_{L \leftarrow L}/s_{L \leftarrow R} & 1/s_{L \leftarrow R} \\ s_{R \leftarrow L} - s_{L \leftarrow L}s_{R \leftarrow R}/s_{L \leftarrow R} & s_{R \leftarrow R}/s_{L \leftarrow R} \end{pmatrix} \quad (\text{S15})$$

We can now obtain the transfer matrix for a system of size $N_{\text{ext}}L$ ($N_{\text{ext}} \in \mathbb{N}_0$) by taking products of transfer matrices:

$$M_{\text{ext}} = M_1 M_2 \cdots M_{N_{\text{ext}}}, \quad (\text{S16})$$

which yields again a 2-by-2 transfer (or scattering) matrix. The transmission probability of the extended system is then given by $p_{\text{ext}} = 1/|M_{\text{ext},2,2}|^2$. The subscript denoting that the system is extended is omitted in the Main Text.

SUPPLEMENTAL NOTE 4. DISORDER AVERAGING

We implement the following disorder averaging scheme for the transmission probability p that enters the conductance matrix in (see [SUPPLEMENTAL NOTE 2](#)) for a system of length $N_{\text{ext}}L$. We calculate the scattering matrix of a system with length L numerically for N_{dis} times (with $N_{\text{dis}} > N_{\text{ext}}$), and pick N_{ext} random and distinct scattering matrices to construct the transfer matrix of the extended system and extract the corresponding transmission probability p_{ext} . We can obtain a disorder-averaged p_{ext} by picking N_{combi} different combinations of N_{ext} scattering matrices (with $N_{\text{combi}} < N_{\text{dis}}!/(N_{\text{dis}} - N_{\text{ext}})!$) and calculating the average over those combinations. The average and standard deviation of p_{ext} are shown as a function of N_{combi} in Fig. S1 and display a well-behaved $1/N^{1/2}$ convergence. For the results presented in the Main Text, we consider the disorder-averaged $\langle p_{\text{ext}} \rangle$ with $N_{\text{ext}} = 20$, $N_{\text{dis}} = 5000$ and $N_{\text{combi}} = 5000$ such that the error δp_{ext} is at most of the order of 1% (see red dotted line in Fig. S1b).

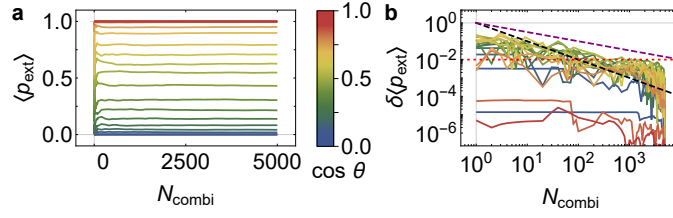
SUPPLEMENTAL NOTE 5. TRANSITION CURVES

For the interpolation of the conductivities $\sigma_{xx,xy}(\cos \theta)$ over the range $\cos \theta \in [0, 1]$, we consider a tanh profile that is fitted to the data points:

$$\sigma_{xy}(\cos \theta) = \{1 + \tanh[(\cos \theta - a)/b]\}/2, \quad (\text{S17})$$

$$\sigma_{xx}(\cos \theta) = \sqrt{1 - (2\sigma_{xy} - 1)^2}/2 = \sqrt{1 - \tanh^2[(\cos \theta - a)/b]}/2, \quad (\text{S18})$$

with fitting parameters a and b . Examples of this interpolation curve are shown in Fig. 1e of the Main Text, which shows that they capture the transition behavior very well. From these fitting parameters, we can extract the transition value $\cos \theta^* = a$ and the maximal slope $\max\{\partial \sigma_{xy}/\partial \cos \theta\} = 1/(2b)$ (see [SUPPLEMENTAL NOTE 7](#)), as well as propagate the uncertainty of the fits for a and b .



Supplemental Figure S1. **Disorder-averaged transmission probability.** (a) The average transmission probability $\langle p_{\text{ext}} \rangle$ as a function of the number of combinations of disorder configurations N_{combi} (see text for details) up to a maximum of $N_{\text{combi}} = 5000$ for different values of $\cos \theta$. (b) The difference of the mean with respect to the overall mean ($\delta \langle p_{\text{ext}} \rangle \equiv |\langle p_{\text{ext}} \rangle_{N_{\text{combi}}} - \langle p_{\text{ext}} \rangle_{5000}|$) as a function of the number of combinations N_{combi} up to a maximum of $N_{\text{combi}} = 5000$ for different values of $\cos \theta$ on a log-log scale. The slope of $1/N_{\text{combi}}^{1/2}$ and $1/N_{\text{combi}}$ is shown for comparison with purple and black dashed lines, respectively. The transmission probabilities here are obtained for an MTI ribbon with $W = 0.05 \mu\text{m}$, $L = 0.2 (4) \mu\text{m}$ ($N_{\text{ext}} = 20$), $E_F = 0.2 E_{\text{gap}}^{\theta=0}$, spatially uncorrelated disorder with $S_{\text{dis}} = 3 E_{\text{gap}}^{\theta=0}$, and magnetization rotated in the x - z plane.

SUPPLEMENTAL NOTE 6. FINITE-SIZE SCALING ANALYSIS BASED ON MACKINNON-KRAMER FITTING PROCEDURE

The standard MacKinnon-Kramer fitting procedure [S1] involves the minimization of the following quantity (adapted to the notation and system under consideration here with $\cos \theta$ instead of a disorder parameter):

$$S = \sum_{i=1}^{N_\lambda} \left[\frac{1}{N_i} \sum_{j=1}^{N_i} [\ln L_{ij} - \ln L_{\text{eff}}(\cos \theta_j)]^2 - \left(\frac{1}{N_i} \sum_{j=1}^{N_i} [\ln L_{ij} - \ln L_{\text{eff}}(\cos \theta_j)] \right)^2 \right], \quad (\text{S19})$$

with i an index for labeling N_λ different localization lengths λ_i (not appearing explicitly in the quantity S) and j an index for labeling N_i different values of $\cos \theta$ in our data set at a given localization length Λ_i . Each pair of indices (i, j) corresponds to a data point for a specific system size (length) L_{ij} that yields localization length λ_j for $\cos \theta = \cos \theta_i$. The minimization yields a discretized relation of effective size L_{eff} as a function of $\cos \theta$ such that the localization length $\lambda(L, \cos \theta)$ follows single-parameter scaling:

$$\lambda(L, \cos \theta) = f[L/L_{\text{eff}}(\cos \theta)]. \quad (\text{S20})$$

Here, we use the terminology *effective size* instead of correlation length (commonly used in the context of phase transitions) to avoid confusion with the correlation length of the disorder potential Λ . From the analytic properties of the function f , it follows that the characteristic length features a power-law divergence close to the phase transition:

$$L_{\text{eff}}(\cos \theta) \propto |\delta \cos \theta|^{-\nu}, \quad (\text{S21})$$

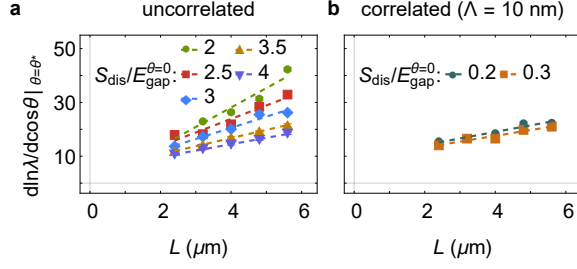
with effective-size exponent ν and $\delta \cos \theta_c \equiv \cos \theta - \cos \theta_c$. The discretized relation for the characteristic length L_{eff} can then be obtained by solving the following set of linear equations:

$$0 = \frac{\delta S}{\delta \ln L_{\text{eff}}(\cos \theta_k)} = 2 \sum_{i=1}^{N_\lambda} \sum_{j=1}^{N_i} \sum_{j'=1}^{N_i} \delta_{kj'} \left[\left(\frac{1}{N_i^2} - \frac{\delta_{kj}}{N_i} \right) \ln L_{ij} + \left(\frac{\delta_{kj}}{N_i} - \frac{1}{N_i^2} \right) \ln L_{\text{eff}}(\cos \theta_j) \right]. \quad (\text{S22})$$

Here, we consider a variation of this approach that treats all data sets (for different system parameters and disorder characteristics), each with a unique set of adaptively sampled $\cos \theta$ values, on equal footing. We start with a system size-dependent dimensionless renormalized localization length extracted from the disorder-averaged transmission probability across the system (see [SUPPLEMENTAL NOTE 4](#)), defined as:

$$\lambda(L, \cos \theta) \equiv -1 / \ln(\langle p_{\text{ext}}(L, \cos \theta) \rangle). \quad (\text{S23})$$

We have numerically obtained data points $\lambda_{kj}(L_k, \cos \theta_j)$ for N_{sys} different systems with different sizes (keeping the aspect ratio fixed), indexed by k , and for a number of $\cos \theta$ values that are indexed by j and adaptively sampled. See Fig. 1e of the Main Text for an example data set with σ_{xx}, σ_{xy} values extracted from the $\langle p_{\text{ext}} \rangle$ values.



Supplemental Figure S2. The slope $d \ln \lambda / d \cos \theta |_{\theta=\theta^*}$ as a function of MTI ribbon length L with (a) spatially uncorrelated and (b) spatially correlated ($\Lambda = 10$ nm) disorder for different disorder strengths S_{dis} , considering an x - z rotation plane and Fermi level $E_F = 0.2 E_{\text{gap}}^{\theta=0}$. A linear fit is shown with dashed lines.

As the transition curve of $\sigma_{xy}(\cos \theta)$ is well described by a tanh profile [see Eq. (S17)], we can apply the curve to derive a continuous expression for $\ln \lambda$ as a function of $\cos \theta$:

$$\sigma_{xy}(\cos \theta) = \{1 + \tanh[(\cos \theta - a)/b]\}/2 = [1 + \tanh(\delta \cos \theta/b)]/2, \quad (\text{S24})$$

$$\rightarrow p(\cos \theta) = \left[1 + \coth(\delta \cos \theta/b) \left(1 - \sqrt{1 - \tanh^2(\delta \cos \theta/b)}\right)\right]/2, \quad (\text{S25})$$

$$\begin{aligned} \rightarrow \lambda(\cos \theta) &= -1/\ln p(\cos \theta) \\ &= -1/\ln \left[1/2 + \coth(\delta \cos \theta/b) \left(1 - \sqrt{1 - \tanh^2(\delta \cos \theta/b)}\right)\right]/2, \end{aligned} \quad (\text{S26})$$

with $\delta \cos \theta \equiv \cos \theta - a$. As we consider the profile of the localization length near the transition value $\cos \theta = a$ with $\lambda(\cos \theta = a) = 1/\ln 2 \equiv \lambda_c$, the profile $\ln \lambda(\delta \cos \theta)$ is a function parametrized by a single parameter b . From Eq. (S26), it follows directly that $d \ln \lambda / d \cos \theta |_{\cos \theta = a}$ is proportional to the inverse of b :

$$d \ln \lambda / d \cos \theta |_{\cos \theta = a} = 1/(b \ln 4). \quad (\text{S27})$$

For the simulated system sizes, the dependence of $1/b$ on system size is well described by a linear relation (see Fig. S2):

$$1/b \approx c_0 + c_1 L, \quad (\text{S28})$$

with c_0 and c_1 depending on the system parameters (e.g., Fermi level) and disorder characteristics (e.g., disorder strength). Substituting this relation, obtained via linear regression of the fits $1/b_k(L_k)$, into Eq. (S26), we obtain:

$$L(\lambda, \delta \cos \theta) = \frac{\text{arctanh}[e^{1/\lambda}(2 - e^{1/\lambda})/(2 - 2e^{1/\lambda} + e^{2/\lambda})] - c_0 \delta \cos \theta}{c_1 \delta \cos \theta}. \quad (\text{S29})$$

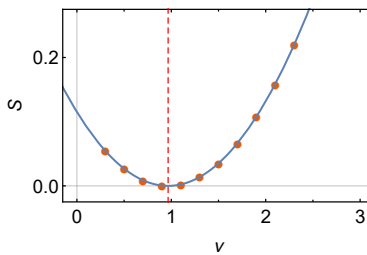
With this relation, we can evaluate a continuum formulation of the quantity S , which becomes a functional of the to-be-determined function $L_{\text{eff}}(\cos \theta)$ and evaluates the variance of $\ln L - \ln L_{\text{eff}}$ over a range of $\cos \theta$ values for a range of $\ln \lambda$ values:

$$\begin{aligned} S[L_{\text{eff}}(\cos \theta)] &\equiv \frac{N_\lambda}{\Delta \ln \lambda} \int_{\ln \lambda_{\min}}^{\ln \lambda_{\max}} d(\ln \lambda) \frac{1}{\delta \cos \theta(\ln \lambda)} \int_{\delta \cos \theta_{\min}(\ln \lambda)}^{\delta \cos \theta_{\max}(\ln \lambda)} d(\delta \cos \theta) [\ln L(\lambda, \delta \cos \theta) - \ln L_{\text{eff}}(\delta \cos \theta)]^2 \\ &- \frac{N_\lambda}{\Delta \ln \lambda} \int_{\ln \lambda_{\min}}^{\ln \lambda_{\max}} d(\ln \lambda) \left(\frac{1}{\delta \cos \theta(\ln \lambda)} \int_{\delta \cos \theta_{\min}(\ln \lambda)}^{\delta \cos \theta_{\max}(\ln \lambda)} d(\delta \cos \theta) [\ln L(\lambda, \delta \cos \theta) - \ln L_{\text{eff}}(\delta \cos \theta)] \right)^2, \end{aligned} \quad (\text{S30})$$

$$\Delta \ln \lambda \equiv \ln \lambda_{\max} - \ln \lambda_{\min}, \quad \delta \cos \theta(\ln \lambda) \equiv \delta \cos \theta_{\max}(\ln \lambda) - \delta \cos \theta_{\min}(\ln \lambda). \quad (\text{S31})$$

As we only have data for system sizes ranging from L_{\min} up to L_{\max} , we get the following integration boundaries for $\cos \theta$:

$$\begin{aligned} \delta \cos \theta(\lambda) &\in [\delta \cos \theta_{\min}(\lambda), \delta \cos \theta_{\max}(\lambda)], \\ \delta \cos \theta_{\min}(\lambda) &\equiv \text{arctanh}[e^{1/\lambda}(2 - e^{1/\lambda})/(2 - 2e^{1/\lambda} + e^{2/\lambda})]/(c_0 + c_1 L_{\max}), \\ \delta \cos \theta_{\max}(\lambda) &\equiv \text{arctanh}[e^{1/\lambda}(2 - e^{1/\lambda})/(2 - 2e^{1/\lambda} + e^{2/\lambda})]/(c_0 + c_1 L_{\min}). \end{aligned}$$



Supplemental Figure S3. The quantity S [Eq. (S32)] evaluated for different values of ν for an MTI ribbon with $E_F = 0.2 E_{\text{gap}}^{\theta=0}$ and spatially uncorrelated disorder with $S_{\text{dis}} = 2 E_{\text{gap}}^{\theta=0}$, considering an x - z magnetization rotation plane (see corresponding localization lengths in Figs. 4a-b of the Main Text). The value of ν for which S is minimized, obtained via quadratic regression (blue curve), is indicated with a vertical red dashed line.

The localization length should be evaluated near the transition and here we consider an interval above the transition with $\ln \lambda \in [\ln \lambda_{\text{min}}, \ln \lambda_{\text{max}}] > \ln \lambda_c$ (the same results are obtained with a similar interval below the transition). For our analysis presented in the Main Text, we have $L_{\text{min}} = 2.4 \mu\text{m}$, $L_{\text{max}} = 5.6 \mu\text{m}$, $\ln \lambda_{\text{min}} = \ln \lambda_c + 0.2$, $\ln \lambda_{\text{max}} = \ln \lambda_c + 1.5$.

Inserting the power-law expression for the effective size in Eq. (S21), we obtain a quantity S that depends only on a single parameter, which is the effective-size exponent ν :

$$S(\nu) \equiv \frac{N_\lambda}{\Delta \ln \lambda} \int d(\ln \lambda) \frac{1}{\delta \cos \theta(\ln \lambda)} \int d(\delta \cos \theta) [\ln L(\lambda, \delta \cos \theta) + \nu \ln |\delta \cos \theta|]^2 - \frac{N_\lambda}{\Delta \ln \lambda} \int d(\ln \lambda) \left(\frac{1}{\delta \cos \theta(\ln \lambda)} \int d(\delta \cos \theta) [\ln L(\lambda, \delta \cos \theta) + \nu \ln |\delta \cos \theta|] \right)^2, \quad (\text{S32})$$

with the same integration boundaries as in Eq. (S30) being understood. This quantity can be evaluated in a straightforward manner via numerical integration and minimized with respect to ν to obtain the effective-size exponent (see example in Fig. S2). The results of the single-parameter minimization are presented in Fig. 4c of the Main Text.

SUPPLEMENTAL NOTE 7. FINITE-SIZE SCALING ANALYSIS BASED ON SLOPE OF TRANSITION CURVE

According to finite-size scaling theory [S2, S3], the conductivity displays single-parameter scaling of the form:

$$\sigma_{\mu\nu}(L_{\text{eff}}, B) = \frac{e^2}{h} f_{\mu\nu}[L_{\text{eff}}^{1/\nu}(B - B_c)], \quad (\text{S33})$$

with L_{eff} the effective system or sample size and ν the effective-size exponent. For our zero-temperature quantum transport simulations of MTI ribbons, the effective size is proportional to the simulated system size ($L_{\text{eff}} \propto L$), whereas the magnetic field can be replaced by the dimensionless parameter $\cos \theta$ that controls the out-of-plane magnetization. Hence, the single-parameter scaling relation translates to:

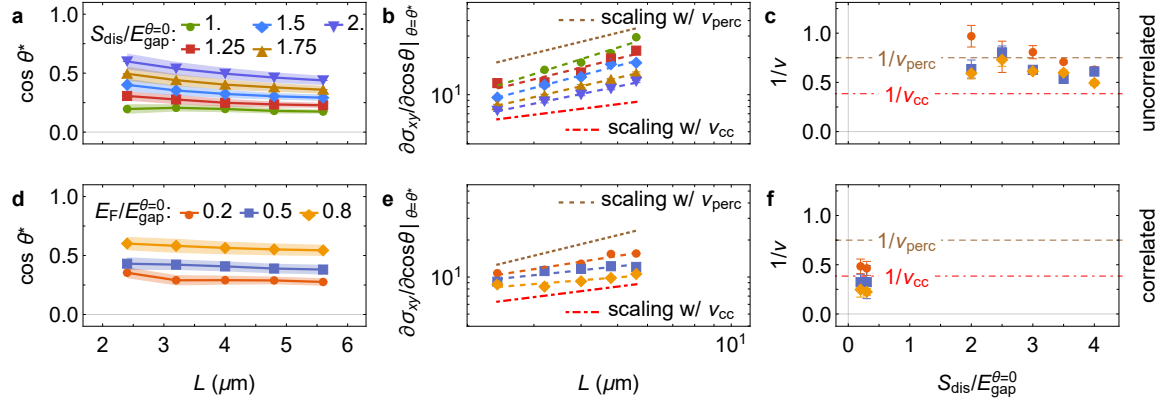
$$\sigma_{xy}(L, \cos \theta) = \frac{1}{2} \frac{e^2}{h} g_{xy}[L^{1/\nu}(\cos \theta - \cos \theta_c)]. \quad (\text{S34})$$

Instead of carrying out the MacKinnon-Kramer fitting procedure, a finite-size scaling analysis can also be performed by tracing the slope $\partial \sigma_{xy} / \partial \cos \theta$ as a function of system size and fitting a power law to this relation [S4]. The critical exponent ν can be extracted from the log-log scaling of the derivative $\partial \sigma_{xy} / \partial \cos \theta|_{\theta=\theta_c}$ as a function of the simulated MTI ribbon length L :

$$\ln \left(\frac{\partial \sigma_{xy}(L, \cos \theta)}{\partial \cos \theta} \Big|_{\theta=\theta_c} \right) = \frac{1}{\nu} \ln L + \ln \left(\frac{1}{2} \frac{e^2}{h} g'_{xy}(0) \right). \quad (\text{S35})$$

We have carried out such an analysis of the slope and the results are presented in Fig. S4. The results are in good agreement with the MacKinnon-Kramer fitting procedure.

Note that, at the transition, the slope of $\ln \lambda$ and of σ_{xy} are proportional, as can be derived from the tanh profile for the transition curve of Eq. (S17): $d \ln \lambda / d \cos \theta|_{\cos \theta=a} = 1/(b \ln 4) \propto d \sigma_{xy} / d \cos \theta|_{\cos \theta=a} = 1/b$.



Supplemental Figure S4. **Size scaling analysis of quantum anomalous Hall-to-trivial insulator transition based on $\max\{\partial\sigma_{xy}/\partial\cos\theta\}$.** (a),(d) The transition value $\cos\theta^*$ as a function of MTI ribbon length L for (a) different disorder strengths S_{dis} (considering spatially uncorrelated disorder) and (d) for different Fermi level positions E_F (considering spatially correlated disorder with $\Lambda = 10$ nm). (b),(e) The maximal slope $\partial\sigma_{xy}/\partial\cos\theta$ as a function of MTI ribbon length for (a) different disorder strengths (considering spatially uncorrelated disorder) and (d) for different positions of the Fermi levels (considering spatially correlated disorder). (c),(f) The inverse of the size-scaling exponent ν as a function of disorder strength for different Fermi level positions, considering (c) spatially uncorrelated and (f) spatially correlated ($\Lambda = 10$ nm) disorder. Scaling curves according to classical ($\nu_{\text{perc}} = 4/3$) and quantum ($\nu_{\text{cc}} = 2.6$) percolation are shown for comparison. The magnetization is rotated in the x - z plane, and the results shown in a,b (d,e) correspond to $E_F = 0.2 E_{\text{gap}}^{\theta=0}$ ($S_{\text{dis}} = 0.2 E_{\text{gap}}^{\theta=0}$).

-
- [S1] A. MacKinnon and B. Kramer, *Z. Phys. B Condens. Matter* **53**, 1 (1983).
[S2] A. M. M. Pruisken, *Phys. Rev. Lett.* **61**, 1297 (1988).
[S3] B. Huckestein, *Rev. Mod. Phys.* **67**, 357 (1995).
[S4] M. Kawamura, M. Mogi, R. Yoshimi, A. Tsukazaki, Y. Kozuka, K. S. Takahashi, M. Kawasaki, and Y. Tokura, *Phys. Rev. B* **102**, 041301 (2020).